Aranda-Iglesias, D.; Vadillo, G.; Rodríguez-Martínez, J.A.; Volokh, K.Y. (2017). Modeling deformation and failure of elastomers at high strain rates. *Mechanics of Materials*, vol. 104, pp. 85-92.

DOI: https://doi.org/10.1016/j.mechmat.2016.10.004

Modeling deformation and failure of elastomers at high strain rates

D. Aranda-Iglesias, G. Vadillo, J.A. Rodríguez-Martínez
Department of Continuum Mechanics and Structural Analysis
University Carlos III of Madrid, Spain

K.Y. Volokh*
Faculty of Civil and Environmental Engineering
Technion – Israel Institute of Technology, Israel

September 8, 2016

Abstract

In this paper we develop a new constitutive model to describe the viscoelastic response of elastomers subjected to high strain rates. The key and original feature of the model is that it takes into account the failure of the material using an energy limiter. We calibrate the constitutive model for various strain rates using the experimental data reported by Hoo Fatt and Ouyang (2008) and show the capacity of the proposed formulation to describe the rate-dependent behavior of styrene butadiene rubber. In addition, we implement the model into ABAQUS/Explicit using a simple scheme for the temporal integration of the constitutive equations. Finally, we show sample numerical simulations to illustrate the joint performance of the constitutive model and the integration algorithm.

1 Introduction

Elastomers are used in tires, isolation bearings, shock absorbers, coatings etc. They can be exposed to shock, vibrations, blast and impact. An elastomer may stretch easily more than 500% under an applied load. Failure of elastomers is a fundamental issue. The breakdown of rubber tires because of the catastrophic crack propagation results in more severe loss of capital and life than airplane accidents. It is apparent that the correct modeling of failure can improve the design of all kinds of parts, components and structures manufactured with rubber-like materials.

Complicated mechanical behavior of long molecular chains underlies the macroscopic response of elastomers including their strain rate dependence. The micro-structural mechanism of the rate-dependence or viscosity is not well understood. Nevertheless, there are various ways to incorporate viscosity in constitutive models of finite elasticity. For example, a plenty of integral formulations of nonlinear viscoelasticity started from Green and Rivlin (1957, 1960). Further developments are reviewed in Lockett (1972); Carreau et al. (1997); Hoo Fatt and Ouyang (2007) and Wineman (2009). There are also numerous differential formulations of nonlinear viscoelasticity based on the introduction of internal variables and their evolution equations: Lubliner (1985); Lion (1996);

*Corresponding author, E-mail: cvolokh@technion.ac.il

Govindjee and Reese (1997); Reese and Govindjee (1998); Bergström and Boyce (1998); Huber and Tsakmakis (2000); Miehe and Keck (2000) and Amin et al. (2006).

All mentioned viscoelasticity theories were developed for relatively low strain rates of about 1 s^{-1}. High strain rates of 1100-3000 s^{-1} for silicone rubber were considered by Yang et al. (2000) and Shim et al. (2004). Strain rates of about 5000 s^{-1} for a filled polybutadiene were studied by Quintavalla and Johnson (2004). Recently, Hoo Fatt and Ouyang (2008) explored the dynamic behavior of styrene butadiene rubber (SBR) and found that its rate-dependence is very limited at sufficiently high strain rates. Importantly and uniquely, experiments by Hoo Fatt and Ouyang (2008) also tracked the changing strength of SBR at varying strain rates.

It is worth noting that most theories considered the intact material behavior, in which the deformation description did not incorporate mechanical failure. However, real materials do fail and their constitutive equations should include a description of failure. In the context of purely elastic deformation (without viscosity) a very simple account of material failure in the constitutive laws was proposed in a series of recent publications: Volokh (2004, 2007, 2010, 2011, 2013b, 2014). The basic idea was to introduce an energy limiter in the expression for strain energy. Such limiter enforces saturation –the failure energy– in the strain energy function, which indicates the maximum amount of energy that can be stored by an infinitesimal material volume prior to rupture.

The mentioned approach of elasticity with energy limiters does not include the viscosity effect. The first attempt to fill this gap was made in Volokh and Trapper (2008) in a very simple quasi-linear integral formulation. The latter theory is limited in applications and more general nonlinear viscoelastic formulation with energy limiters is desirable. Thus, in the present paper we: (1) develop a new constitutive model which includes material failure to describe the viscous response of rubber at high strain rates, (2) calibrate the model for various strain rates using the experimental data reported by Hoo Fatt and Ouyang (2008), (3) implement the novel constitutive theory into ABAQUS/Explicit via a user subroutine and (4) show the performance of the model in a series of numerical examples. It is worth emphasizing that our formulation is by no means unique and it has to be understood as a starting point to provide new insights into the (largely unexplored) rate dependent deformation and failure behaviour of rubber like materials.

2 Nonlinear viscoelasticity with energy limiters

2.1 Basic equations

Consider a material point that occupies position $\mathbf{X}$ in the reference configuration Ω_0 of a deformable body. The current position vector $\mathbf{x}$ in the deformed configuration Ω is given by $\mathbf{x}= \boldsymbol{\chi}(\mathbf{X}, \mathrm{t})$, where $\boldsymbol{\chi}$ is a bijective and twice continuously differentiable mapping. Deformation in the vicinity of the material point is described by the deformation gradient tensor $\mathbf{F}$

$$\mathbf{F} = \frac{\partial \mathbf{x}}{\partial \mathbf{X}} \tag{1}$$

The linear and angular momentum balance take the following forms accordingly

$$\mathrm{div}\boldsymbol{\sigma} + \mathbf{b} = \rho \mathbf{a} \tag{2}$$

$$\boldsymbol{\sigma} = \boldsymbol{\sigma}^{\mathrm{T}} \tag{3}$$

where the divergence operator is calculated with respect to the current coordinates $\mathbf{x}$, $\boldsymbol{\sigma}$ is the Cauchy stress tensor, $\mathbf{b}$ is the body force pure unit of current volume, ρ and $\mathbf{a}$ are the current mass density and acceleration vector correspondingly.

Balance of linear momentum on the body surface $\partial\Omega$ reads

$$\boldsymbol{\sigma}\mathbf{n} = \bar{\mathbf{t}} \tag{4}$$

where $\bar{\mathbf{t}}$ is a prescribed traction per unit area of the surface with the unit outward normal $\mathbf{n}$.

Alternatively to (4) a surface boundary condition can be imposed on placements

$$\mathbf{x} = \bar{\mathbf{x}} \tag{5}$$

where $\bar{\mathbf{x}}$ is prescribed on the surface $\partial\Omega$.

Initial conditions are

$$\mathbf{x}(\mathrm{t}=0) = \mathbf{x}_0, \quad \mathbf{v}(\mathrm{t}=0) = \mathbf{v}_0 \tag{6}$$

where $\mathbf{v}$ is the velocity vector and $\mathbf{x}_0$ and $\mathbf{v}_0$ are prescribed in Ω.

2.2 Constitutive model

In the present work we adapt the Eulerian constitutive framework for large inelastic deformations developed by Volokh (2013a) for a description of isotropic finite viscoelasticity with energy limiters. We assume that the *standard solid* rheological model underlies the constitutive equations, see Fig. 1.

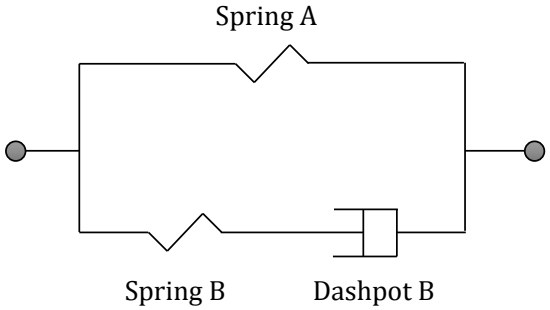

Figure 1: Rheological model of the *standard solid*.

We assume an aditive decomposition of the strain energy function of the form

$$\psi(\mathbf{B}, \mathbf{B}_\mathrm{B}, \xi) = \psi_\mathrm{A}(\mathbf{B}, \xi) + \psi_\mathrm{B}(\mathbf{B}_\mathrm{B}, \xi) \tag{7}$$

where ψ_A is the strain energy function of the spring A which serves to characterize the thermodynamic equilibrium states of the elastomer and ψ_B is the strain energy function of the spring B which serves to account for the additional energy storage and non-equilibrium states. Furthermore, $\mathbf{B} = \mathbf{F}\mathbf{F}^\mathrm{T}$ is the left Cauchy-Green strain tensor, $\mathbf{B}_\mathrm{B}$ is an (strain like) internal variable of the model and ξ is a switch parameter (that will be defined later). We further impose the following conditions on the strain energy function of spring A

$$\psi_\mathrm{A}(\mathbf{B}, \xi) = \psi_\mathrm{A}^\mathrm{f} - \mathrm{H}(\xi)\psi_\mathrm{A}^\mathrm{e}(\mathbf{B}) \tag{8}$$

$$\psi_\mathrm{A}^\mathrm{f} = \psi_\mathrm{A}^\mathrm{e}(\mathbf{1}) \tag{9}$$

$$\|\mathbf{B}\| \to \infty \Rightarrow \psi_\mathrm{A}^\mathrm{e}(\mathbf{B}) \to 0 \tag{10}$$

where $\psi_\mathrm{A}^\mathrm{f}$ and $\psi_\mathrm{A}^\mathrm{e}(\mathbf{B})$ designate the constant bulk failure energy and the elastic free energy of the spring A, respectively. Moreover, $\mathrm{H}(\xi)$ is a unit step function, i.e. $\mathrm{H}(\mathrm{z}) = 0$ if $\mathrm{z} < 0$ and $\mathrm{H}(\mathrm{z}) = 1$ otherwise; $\mathbf{1}$ is a second-order identity tensor; and $\|...\|$ is a tensor norm.

The switch parameter $\xi \in (-\infty, 0]$ is defined by the evolution equation

$$\dot{\xi} = -\mathrm{H}\left(\varepsilon - \frac{\psi_{\mathrm{A}}^{\mathrm{e}}}{\psi_{\mathrm{A}}^{\mathrm{f}}}\right), \quad \xi(\mathrm{t}=0) = 0 \tag{11}$$

where $0 < \varepsilon \ll 1$ is a dimensionless precision constant.

The physical interpretation of the strain energy function is straightforward: the response of the spring A is elastic as long as the strain energy is below its limit, $\psi_{\mathrm{A}}^{\mathrm{f}}$. When the limit is reached, the strain energy remains constant for the rest of the deformation process, thereby making material healing impossible. The parameter ξ is *not* an internal variable (like in Damage Mechanics); it works as a switch: if $\xi = 0$ then the process is elastic and if $\xi < 0$ then the material is irreversibly damaged and the stored energy is dissipated.

In order to enforce the energy limiter in the strain energy function, we use the following form of the elastic energy

$$\psi_{\mathrm{A}}^{\mathrm{e}}(\mathbf{B}) = \frac{\Phi}{\mathrm{m}} \mathit{\Gamma}\left(\frac{1}{\mathrm{m}}, \frac{\mathrm{W_A}(\mathbf{B})^{\mathrm{m}}}{\Phi^{\mathrm{m}}}\right) \tag{12}$$

where $\mathit{\Gamma}(\mathrm{s}, \mathrm{x}) = \int_{\mathrm{x}}^{\infty} \mathrm{t}^{\mathrm{s}-1}\mathrm{e}^{-\mathrm{t}}\mathrm{dt}$ is the upper incomplete gamma function, $\mathrm{W_A}(\mathbf{B})$ is the strain energy of *intact* material, Φ is the energy limiter and m is a dimensionless material parameter which controls the sharpness of the transition to material failure in the stress-strain curve. Increasing or decreasing m it is possible to simulate more or less steep ruptures of the internal bonds accordingly.

The failure energy can be calculated as follows

$$\psi_{\mathrm{A}}^{\mathrm{f}} = \psi_{\mathrm{A}}^{\mathrm{e}}(\mathbf{1}) = \frac{\Phi}{\mathrm{m}} \mathit{\Gamma}\left(\frac{1}{\mathrm{m}}, \frac{\mathrm{W_A}(\mathbf{1})^{\mathrm{m}}}{\Phi^{\mathrm{m}}}\right) \tag{13}$$

Note that the failure energy is a constant that depends on the two failure parameters (Φ, m) through the gamma function. There is no need to limit the energy of spring B as long as the failure of spring A leads to the overall failure. Therefore, we define the strain energy function for the spring B as

$$\psi_{\mathrm{B}}(\mathbf{B}_{\mathrm{B}}, \xi) = \mathrm{H}(\xi)\mathrm{W_B}(\mathbf{B}_{\mathrm{B}}) \tag{14}$$

where $\mathrm{W_B}(\mathbf{B}_{\mathrm{B}})$ stands for the strain energy without failure. Note that this formulation is valid for any pair of strain energies $\mathrm{W_A}$ and $\mathrm{W_B}$ used to describe the intact behavior of the material.

Based on the additive decomposition of the strain energy function ψ, the Cauchy stress is given by

$$\boldsymbol{\sigma} = \boldsymbol{\sigma}_{\mathrm{A}} + \boldsymbol{\sigma}_{\mathrm{B}} \tag{15}$$

where

$$\boldsymbol{\sigma}_{\mathrm{A}} = 2\mathrm{I}_3^{-1/2} \frac{\partial \psi_{\mathrm{A}}}{\partial \mathbf{B}} \mathbf{B} = 2\mathrm{I}_3^{-1/2} \left(\mathrm{I}_3 \psi_3 \mathbf{1} + (\psi_1 + \mathrm{I}_1 \psi_2)\, \mathbf{B} - \psi_2 \mathbf{B}^2\right) \tag{16}$$

$$\boldsymbol{\sigma}_{\mathrm{B}} = 2\mathrm{I}_{\mathrm{B3}}^{-1/2} \frac{\partial \psi_{\mathrm{B}}}{\partial \mathbf{B}_{\mathrm{B}}} \mathbf{B}_{\mathrm{B}} = 2\mathrm{I}_{\mathrm{B3}}^{-1/2} \left(\mathrm{I}_{\mathrm{B3}} \psi_{\mathrm{B3}} \mathbf{1} + (\psi_{\mathrm{B1}} + \mathrm{I}_{\mathrm{B1}} \psi_{\mathrm{B2}})\, \mathbf{B}_{\mathrm{B}} - \psi_{\mathrm{B2}} \mathbf{B}_{\mathrm{B}}^2\right) \tag{17}$$

The principal invariants are given by

$$\mathrm{I}_1 = \mathrm{tr}\mathbf{B}, \quad 2\mathrm{I}_2 = (\mathrm{tr}\mathbf{B})^2 - \mathrm{tr}\,(\mathbf{B})^2, \quad \mathrm{I}_3 = \mathrm{det}\mathbf{B} \tag{18}$$

$$\mathrm{I}_{\mathrm{B1}} = \mathrm{tr}\mathbf{B}_{\mathrm{B}}, \quad 2\mathrm{I}_{\mathrm{B2}} = (\mathrm{tr}\mathbf{B}_{\mathrm{B}})^{\,2} - \mathrm{tr}\,(\mathbf{B}_{\mathrm{B}})^2, \quad \mathrm{I}_{\mathrm{B3}} = \mathrm{det}\mathbf{B}_{\mathrm{B}} \tag{19}$$

and we use the shot notation $\psi_{\mathrm{i}} = \partial\psi/\partial \mathrm{I}_{\mathrm{i}}$ and $\psi_{\mathrm{Bi}} = \partial\psi/\partial \mathrm{I}_{\mathrm{Bi}}$.

The constitutive law (flow rule) for the dashpot is written in the following general form

$$\boldsymbol{\sigma}_{\mathrm{B}} = \beta_1 \mathbf{1} + \beta_2 \mathbf{D}_{\mathrm{B}} + \beta_3 \mathbf{D}_{\mathrm{B}}^2 \tag{20}$$

where $\beta_{\rm i}$ is a function(al), generally, depending on stresses and strains, and $\mathbf{D}_{\rm B}$ is the rate of deformation tensor corresponding to the dashpot.

Following Eckart (1948), Leonov (1976) and Volokh (2013a), we introduce the following evolution equation which relates $\mathbf{B}_{\rm B}$ and $\mathbf{D}_{\rm B}$

$$\overset{\triangledown}{\mathbf{B}}_{\rm B}+\mathbf{D}_{\rm B}\mathbf{B}_{\rm B}+\mathbf{B}_{\rm B}\mathbf{D}_{\rm B}=\mathbf{0},\quad \mathbf{B}_{\rm B}({\rm t}=0)=\mathbf{1} \tag{21}$$

where

$$\overset{\triangledown}{\mathbf{B}}_{\rm B}=\dot{\mathbf{B}}_{\rm B}-\mathbf{L}\mathbf{B}_{\rm B}-\mathbf{B}_{\rm B}\mathbf{L}^{\rm T} \tag{22}$$

is the Oldroyd objective rate of the (strain like) internal variable $\mathbf{B}_{\rm B}$. In previous expression $\mathbf{L}$ refers to the velocity gradient tensor of the whole model.

2.3 Thermodynamic restrictions

We write the Clausius–Duhem dissipation inequality in the following form

$$(\boldsymbol{\sigma}_{\rm A}+\boldsymbol{\sigma}_{\rm B}):\mathbf{D}-{\rm I}_3^{-1/2}\frac{\partial\psi}{\partial\mathbf{B}}:\dot{\mathbf{B}}-{\rm I}_{\rm B3}^{-1/2}\frac{\partial\psi}{\partial\mathbf{B}_{\rm B}}:\dot{\mathbf{B}}_{\rm B}\geq 0 \tag{23}$$

where $\mathbf{D}$ is the strain rate measure corresponding to the whole model.

The second and third terms in previous expression can be rewritten as

$${\rm I}_3^{-1/2}\frac{\partial\psi}{\partial\mathbf{B}}:\dot{\mathbf{B}}=2{\rm I}_3^{-1/2}\frac{\partial\psi}{\partial\mathbf{B}}\mathbf{B}:\mathbf{D} \tag{24}$$

$${\rm I}_{\rm B3}^{-1/2}\frac{\partial\psi}{\partial\mathbf{B}_{\rm B}}:\dot{\mathbf{B}}_{\rm B}=2{\rm I}_{\rm B3}^{-1/2}\frac{\partial\psi}{\partial\mathbf{B}_{\rm B}}\mathbf{B}_{\rm B}:\mathbf{D}-2{\rm I}_{\rm B3}^{-1/2}\frac{\partial\psi}{\partial\mathbf{B}_{\rm B}}\mathbf{B}_{\rm B}:\mathbf{D}_{\rm B} \tag{25}$$

where the relations $\dot{\mathbf{B}}=\mathbf{L}\mathbf{B}+\mathbf{B}\mathbf{L}^{\rm T}$ and $\dot{\mathbf{B}}_{\rm B}=\mathbf{B}_{\rm B}\left(\mathbf{L}-\mathbf{D}_{\rm B}\right)^{\rm T}+\left(\mathbf{L}-\mathbf{D}_{\rm B}\right)\mathbf{B}_{\rm B}$ (the latter is derived from equations (21) and (22)) have been used.

Substitution of (24) and (25) in (23) yields

$$\left(\boldsymbol{\sigma}_{\rm A}-2{\rm I}_3^{-1/2}\frac{\partial\psi}{\partial\mathbf{B}}\mathbf{B}+\boldsymbol{\sigma}_{\rm B}-2{\rm I}_{\rm B3}^{-1/2}\frac{\partial\psi}{\partial\mathbf{B}_{\rm B}}\mathbf{B}_{\rm B}\right):\mathbf{D}+2{\rm I}_{\rm B3}^{-1/2}\frac{\partial\psi}{\partial\mathbf{B}_{\rm B}}\mathbf{B}_{\rm B}:\mathbf{D}_{\rm B}\geq 0 \tag{26}$$

Using the constitutive equations (16) and (17), previous equation reduces to

$$\boldsymbol{\sigma}_{\rm B}:\mathbf{D}_{\rm B}\geq 0 \tag{27}$$

Substituting the flow rule (20) in the latter inequality we get the final thermodynamic restriction

$$\beta_1{\rm tr}\mathbf{D}_{\rm B}+\beta_2{\rm tr}\mathbf{D}_{\rm B}^2+\beta_3{\rm tr}\mathbf{D}_{\rm B}^3\geq 0. \tag{28}$$

As pointed out by Volokh (2013a), an alternative formulation for the constitutive model could be developed using the multiplicative decomposition of the deformation gradient tensor into elastic and viscous parts. Nevertheless, the difference between the present formulation and the alternative based on the multiplicative decomposition of $\mathbf{F}$ is mostly formal: the expressions for the stresses remain unchanged.

2.4 Specialization to incompressible and compressible materials

In this section we specialize the constitutive formulation to incompressible and (slightly) compressible materials. The hypothesis of incompressibility is used in section 3 to approach analytically the uniaxial tension problem and calibrate the constitutive model. Compressibility of the material is taken into account in section 4 to integrate the constitutive equations and implement the model into a finite element code.

2.4.1 Incompressible formulation

The incompressibility condition implies that det$\mathbf{B}$= 1, det$\mathbf{B}_{\mathrm{B}}$= 1 and tr$\mathbf{D}_{\mathrm{B}}$= 0. The constitutive laws for the springs (16) - (17) are written as follows

$$\boldsymbol{\sigma}_{\mathrm{A}} = -\mathrm{p}_{\mathrm{A}}\mathbf{1} + 2\left(\psi_1 + \mathrm{I}_1\psi_2\right)\mathbf{B} - 2\psi_2\mathbf{B}^2 \tag{29}$$

$$\boldsymbol{\sigma}_{\mathrm{B}} = -\mathrm{p}_{\mathrm{B}}\mathbf{1} + 2\left(\psi_{\mathrm{B}1} + \mathrm{I}_{\mathrm{B}1}\psi_{\mathrm{B}2}\right)\mathbf{B}_{\mathrm{B}} - 2\psi_{\mathrm{B}2}\mathbf{B}_{\mathrm{B}}^2 \tag{30}$$

where p_{A} and p_{B} are undefined Lagrange multipliers enforcing incompressibility.

The constitutive law for the dashpot (20) is written in the following simple form

$$\beta_1 = \frac{1}{3}\mathrm{tr}\boldsymbol{\sigma}_{\mathrm{B}}, \quad \beta_2 = \eta_2, \quad \beta_3 = 0 \tag{31}$$

where η_2 is the only viscosity parameter or function.

Substitution of (31) in (20) leads to

$$\boldsymbol{\sigma}_{\mathrm{B}} = \frac{1}{3}\left(\mathrm{tr}\boldsymbol{\sigma}_{\mathrm{B}}\right)\mathbf{1} + \eta_2\mathbf{D}_{\mathrm{B}} \tag{32}$$

Substitution of (32) in (27) yields

$$\eta_2\mathrm{tr}\mathbf{D}_{\mathrm{B}}^2 \geq 0 \tag{33}$$

This dissipation inequality is obeyed imposing the following restriction on the viscosity

$$\eta_2 \geq 0 \tag{34}$$

2.4.2 Compressible formulation

Material compressibility is required to implement the constitutive equations into a numerical code. The constitutive laws for the springs (16) - (17) are written as follows

$$\boldsymbol{\sigma}_{\mathrm{A}} = 2\mathrm{I}_3^{-1/2}\left(\left(\mathrm{I}_3\mathrm{a} - \mathrm{b}\right)\mathbf{1} + \left(\psi_1 + \mathrm{I}_1\psi_2\right)\mathbf{B} - \psi_2\mathbf{B}^2\right) \tag{35}$$

$$\boldsymbol{\sigma}_{\mathrm{B}} = 2{\mathrm{I}_{\mathrm{B}3}}^{-1/2}\left(\left(\mathrm{I}_{\mathrm{B}3}\mathrm{a}_{\mathrm{B}} - \mathrm{b}_{\mathrm{B}}\right)\mathbf{1} + \left(\psi_{\mathrm{B}1} + \mathrm{I}_{\mathrm{B}1}\psi_{\mathrm{B}2}\right)\mathbf{B}_{\mathrm{B}} - \psi_{\mathrm{B}2}\mathbf{B}_{\mathrm{B}}^2\right) \tag{36}$$

where a, b and a_{B},b_{B} are the penalizing bulk moduli for springs A and B, respectively (see Trapper and Volokh (2010)).

We note that the bulk moduli are not independent and they should obey the conditions of zero stress for $\mathbf{B} = \mathbf{B}_{\mathrm{B}} = \mathbf{1}$ and $\mathbf{D} = \mathbf{0}$

$$0 = \mathrm{a} - \mathrm{b} + \psi_1 + 2\psi_2, \quad 0 = \mathrm{a}_{\mathrm{B}} - \mathrm{b}_{\mathrm{B}} + \psi_{\mathrm{B}1} + 2\psi_{\mathrm{B}2} \tag{37}$$

Thus, choosing (for $\mathbf{B} = \mathbf{B}_{\mathrm{B}} = \mathbf{1}$ and $\mathbf{D} = \mathbf{0}$)

$$\mathrm{a} \approx \mathrm{b} \gg \psi_1 + 2\psi_2, \quad \mathrm{a}_{\mathrm{B}} \approx \mathrm{b}_{\mathrm{B}} \gg \psi_{\mathrm{B}1} + 2\psi_{\mathrm{B}2} \tag{38}$$

it is possible to enforce incompressibility in computations.

Following Reese and Govindjee (1998), we write the constitutive law for the dashpot as

$$\beta_1 = \frac{3\eta_1 - 2\eta_2}{9\eta_1}\mathrm{tr}\boldsymbol{\sigma}_{\mathrm{B}}, \quad \beta_2 = \eta_2, \quad \beta_3 = 0 \tag{39}$$

where η_1 and η_2 are two viscosity parameters or functions.

Substitution of (39) in (20) leads to

$$\boldsymbol{\sigma}_{\mathrm{B}} = \frac{3\eta_1 - 2\eta_2}{9\eta_1}(\mathrm{tr}\boldsymbol{\sigma}_{\mathrm{B}})\mathbf{1} + \eta_2 \mathbf{D}_{\mathrm{B}} \tag{40}$$

Substitution of (40) in (27) yields

$$\frac{6\eta_1 - 4\eta_2}{27\eta_1}(\mathrm{tr}\boldsymbol{\sigma}_{\mathrm{B}})^2 + \eta_2 \mathrm{tr}\mathbf{D}_{\mathrm{B}}{}^2 \geq 0 \tag{41}$$

This dissipation inequality is obeyed imposing the following restrictions on the viscosities

$$\eta_2 \geq 0, \quad 3\eta_1 > 2\eta_2 \tag{42}$$

Furthermore, to enhance incompressibility we can impose $\eta_1 >> \eta_2$.

3 Calibration of the constitutive model

In this section the (incompressible) constitutive model is calibrated to describe the mechanical behavior of styrene butadiene rubber. For the calibration we use dynamic tensile tests for various stretch rates performed by Hoo Fatt and Ouyang (2008). Therefore, we restrict our attention to the case when then material undergoes uniaxial tension

$$\mathbf{x} = \lambda \mathrm{X}_1 \mathbf{e}_1 + \lambda^{-1/2}(\mathrm{X}_2 \mathbf{e}_2 + \mathrm{X}_3 \mathbf{e}_3) \tag{43}$$

The left Cauchy-Green tensor $\mathbf{B}$ and the internal variable $\mathbf{B}_{\mathrm{B}}$ admit the spectral representations

$$\mathbf{B} = \lambda^2 \mathbf{e}_1 \otimes \mathbf{e}_1 + \lambda^{-1}(\mathbf{e}_2 \otimes \mathbf{e}_2 + \mathbf{e}_3 \otimes \mathbf{e}_3) \tag{44}$$

$$\mathbf{B}_{\mathrm{B}} = \lambda_{\mathrm{B}}^2 \mathbf{e}_1 \otimes \mathbf{e}_1 + \lambda_{\mathrm{B}}^{-1}(\mathbf{e}_2 \otimes \mathbf{e}_2 + \mathbf{e}_3 \otimes \mathbf{e}_3) \tag{45}$$

which fulfill the incompressibility conditions: $\det\mathbf{B} = 1$ and $\det\mathbf{B}_{\mathrm{B}} = 1$.

Consequently, the stress-stretch curve, $\sigma \sim \lambda$, is given by the following equation

$$\sigma = 2\left(\lambda^2 - \lambda^{-1}\right)\left(\psi_1 + \lambda^{-1}\psi_2\right) + 2\left(\lambda_{\mathrm{B}}^2 - \lambda_{\mathrm{B}}^{-1}\right)\left(\psi_{\mathrm{B1}} + \lambda_{\mathrm{B}}^{-1}\psi_{\mathrm{B2}}\right) \tag{46}$$

where, $\lambda_{\mathrm{B}}(\mathrm{t})$ is given by the following evolution equation

$$\dot{\lambda}_{\mathrm{B}} = \dot{\lambda}\lambda^{-1}\lambda_{\mathrm{B}} - \frac{4\lambda_{\mathrm{B}}}{3\eta_2}\left(\lambda_{\mathrm{B}}^2 - \lambda_{\mathrm{B}}^{-1}\right)\left(\psi_{\mathrm{B1}} + \lambda_{\mathrm{B}}^{-1}\psi_{\mathrm{B2}}\right) = 0,\ \lambda_{\mathrm{B}}(\mathrm{t} = 0) = 1 \tag{47}$$

In the case of steady stretching $\lambda = 1 + \dot{\lambda}\mathrm{t}$, with constant $\dot{\lambda}$, the evolution equation can be rewritten as follows

$$\frac{\mathrm{d}\lambda_{\mathrm{B}}}{\mathrm{d}\lambda} = \lambda^{-1}\lambda_{\mathrm{B}} - \frac{4\lambda_{\mathrm{B}}}{3\eta_2\dot{\lambda}}\left(\lambda_{\mathrm{B}}^2 - \lambda_{\mathrm{B}}^{-1}\right)\left(\psi_{\mathrm{B1}} + \lambda_{\mathrm{B}}^{-1}\psi_{\mathrm{B2}}\right) = 0,\ \lambda_{\mathrm{B}}(\lambda = 1) = 1 \tag{48}$$

We use the formulation proposed by Lopez-Pamies (2010) for the intact strain energy functions

$$\mathrm{W}_{\mathrm{A}}(\mathbf{B}) = \frac{3^{1-\alpha_1}}{2\alpha_1}\mu_1\left(\mathrm{I}_1^{\alpha_1} - 3^{\alpha_1}\right) + \frac{3^{(1-\alpha_2)}}{2\alpha_2}\mu_2\left(\mathrm{I}_1^{\alpha_2} - 3^{\alpha_2}\right) \tag{49}$$

$$\mathrm{W}_{\mathrm{B}}(\mathbf{B}_{\mathrm{B}}) = \frac{3^{1-\alpha_{\mathrm{B1}}}}{2\alpha_{\mathrm{B1}}}\mu_{\mathrm{B1}}\left(\mathrm{I}_{\mathrm{B1}}^{\alpha_{\mathrm{B1}}} - 3^{\alpha_{\mathrm{B1}}}\right) + \frac{3^{(1-\alpha_{\mathrm{B2}})}}{2\alpha_{\mathrm{B2}}}\mu_{\mathrm{B2}}\left(\mathrm{I}_{\mathrm{B1}}^{\alpha_{\mathrm{B2}}} - 3^{\alpha_{\mathrm{B2}}}\right) \tag{50}$$

The viscosity function is taken from Hoo Fatt and Ouyang (2008)

$$\eta_2 = \left(\mathrm{C}_1\left(1-\exp\left(\mathrm{C}_2(\mathrm{I}_1-3)\right)\right)+\mathrm{C}_3\right)\left(\mathrm{C}_4\mathrm{I}_{\mathrm{B1}}^3+\mathrm{C}_5\mathrm{I}_{\mathrm{B1}}^2+\mathrm{C}_6\mathrm{I}_{\mathrm{B1}}+\mathrm{C}_7\right) \tag{51}$$

Thus, the proposed model contains 17 parameters: six for spring A (μ_1, μ_2, α_1, α_2, m, Φ), four for spring B (μ_{B1}, μ_{B2}, α_{B1}, α_{B2}) and seven for the dashpot (C_1, C_2, C_3, C_4, C_5, C_6, C_7), see Table 1. The calibration process developed in this paper consists in two stages. In the first stage, the 15 visco-elastic parameters are determined by fitting simultaneously the experimental data reported by Hoo Fatt and Ouyang (2008) for various stretch rates: $76\,\mathrm{s}^{-1}$, $110\,\mathrm{s}^{-1}$, $150\,\mathrm{s}^{-1}$, $300\,\mathrm{s}^{-1}$, $370\,\mathrm{s}^{-1}$and $450\,s^{-1}$. The genetic algorithm and the non-linear unconstrained minimization algorithm (fminsearch) inbuilt in the MATLAB Optimization Toolbox have been used for this task. It is important to note that this method does not warrantee a global optimal solution. Nevertheless, the agreement between the model and the experimental results is very good. In the second stage, the energy limit Φ is directly determined from the failure stretch and the parameter m is selected depending on the desired sharpness of the transition to material failure in the stress-strain curve.

A salient feature of the energy limiter formulation is its simplicity and applicability to already existing visco-elastic models. Note that the calibration of the two failure parameters is decoupled from the rest of the model.

Spring A

μ_1[MPa]	α_1	μ_2[MPa]	α_2	m	Φ[MPa]
0.391	1.045	2.162	−3.065	30	7.5

Spring B

μ_{B1}[MPa]	α_{B1}	μ_{B2}[MPa]	α_{B2}
3.99	0.382	2.868	−11.295

Dashpot B

C_1[MPa·s]	C_2	C_3[MPa·s]
23.095	$7.421\cdot10^{-8}$	$-8.458\cdot10^{-7}$

C_4	C_5	C_6	C_7
−872.52	−7975.595	22150.457	27310.182

Table 1: Material parameters for SBR rubber.

Figure 2 shows the comparison between the proposed constitutive model (solid lines) and the experiments (markers) reported by Hoo Fatt and Ouyang (2008). Results are shown for various stretch rates. While the material flow stress significantly increases with strain rate, the failure stretch is largely constant for all the loading rates investigated. These experimental observations are properly captured by the constitutive model which shows satisfactory agreement with the experimental evidence for all the loading conditions investigated. Note that our model captures the saturation of the material viscosity at high strain rates.

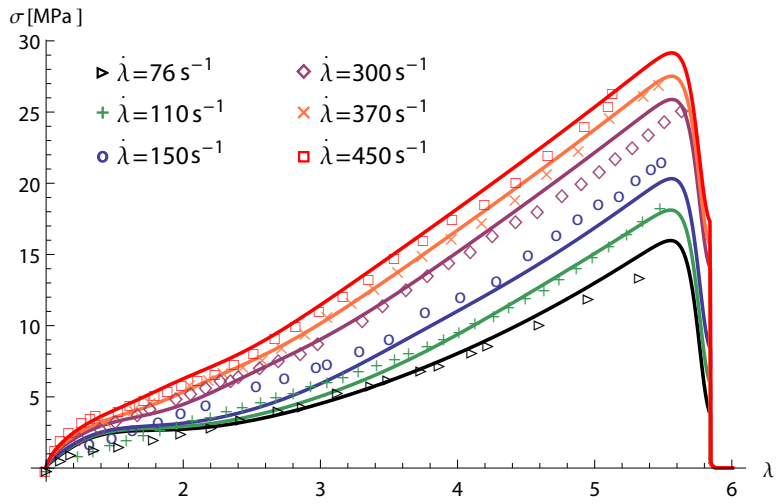

Figure 2: Comparison between the predictions of the constitutive model (solid lines) and the experiments (markers) performed by Hoo Fatt and Ouyang (2008). Uniaxial (Cauchy) stress-stretch curves ($\sigma - \lambda$). A wide range of stretch rates is explored: $76\,\mathrm{s}^{-1}$, $110\,\mathrm{s}^{-1}$, $150\,\mathrm{s}^{-1}$, $300\,\mathrm{s}^{-1}$, $370\,\mathrm{s}^{-1}$ and $450\,s^{-1}$.

4 Finite element implementation

In this section we develop a simple integration algorithm to implement the (slightly compressible) constitutive model into ABAQUS/Explicit code via a user subroutine. The code provides all variables at time t^{n} and the deformation gradient for time $\mathrm{t}^{\mathrm{n+1}}$. The goal is to update all variables of the constitutive model at time $\mathrm{t}^{\mathrm{n+1}}$.

For that purpose we need to integrate equation (21) which provides a relation between the time evolution of the (strain like) internal variable $\overset{\triangledown}{\mathbf{B}}_{\mathrm{B}}$ and the strain rate in the dashpot $\mathbf{D}_{\mathrm{B}}$. The idea of the integration comes from the standard notion that the Oldroyd objective rate can be written with respect to an *arbitrary* reference configuration $\mathbf{z}$ in the following form

$$\overset{\triangledown}{\mathbf{B}}_{\mathrm{B}} = \dot{\mathbf{B}}_{\mathrm{B}} - \mathbf{L}\mathbf{B}_{\mathrm{B}} - \mathbf{B}_{\mathrm{B}}\mathbf{L}^{\mathrm{T}} = \mathbf{K}\left(\frac{\partial}{\partial \mathrm{t}}\left(\mathbf{K}^{-1}\mathbf{B}_{\mathrm{B}}\mathbf{K}^{-\mathrm{T}}\right)\right)\mathbf{K}^{\mathrm{T}} \tag{52}$$

where

$$\mathbf{K} = \frac{\partial \mathbf{x}}{\partial \mathbf{z}};\ \mathbf{L} = \frac{\partial \mathbf{v}}{\partial \mathbf{z}}\frac{\partial \mathbf{z}}{\partial \mathbf{x}} = \dot{\mathbf{K}}\mathbf{K}^{-1} \tag{53}$$

Substitution of (52) in (21) yields

$$\mathbf{K}\left(\frac{\partial}{\partial \mathrm{t}}\left(\mathbf{K}^{-1}\mathbf{B}_{\mathrm{B}}\mathbf{K}^{-\mathrm{T}}\right)\right)\mathbf{K}^{\mathrm{T}} = -\mathbf{D}_{\mathrm{B}}\mathbf{B}_{\mathrm{B}} - \mathbf{B}_{\mathrm{B}}\mathbf{D}_{\mathrm{B}} \tag{54}$$

with the initial condition $\mathbf{B}_{\mathrm{B}}(\mathrm{t}=0) = \mathbf{1}$.

Using the Euler explicit approximation of the time derivative within the interval $[\mathrm{t}^{\mathrm{n}}, \mathrm{t}^{\mathrm{n+1}}]$ and taking into account that $\mathbf{D}_{\mathrm{B}}\mathbf{B}_{\mathrm{B}} = \mathbf{B}_{\mathrm{B}}\mathbf{D}_{\mathrm{B}}$ we get

$$\left(\mathbf{K}^{\mathrm{n+1}}\right)^{-1}\mathbf{B}_{\mathrm{B}}^{\mathrm{n+1}}\left(\mathbf{K}^{\mathrm{n+1}}\right)^{-\mathrm{T}} - \left(\mathbf{K}^{\mathrm{n}}\right)^{-1}\mathbf{B}_{\mathrm{B}}^{\mathrm{n}}\left(\mathbf{K}^{\mathrm{n}}\right)^{-\mathrm{T}} = -2(\mathrm{t}^{\mathrm{n+1}} - \mathrm{t}^{\mathrm{n}})\left(\mathbf{K}^{\mathrm{n}}\right)^{-1}\mathbf{D}_{\mathrm{B}}^{\mathrm{n}}\mathbf{B}_{\mathrm{B}}^{\mathrm{n}}\left(\mathbf{K}^{\mathrm{n}}\right)^{-\mathrm{T}} \tag{55}$$

in which we designated

$$(\bullet)(\mathrm{t}^{\mathrm{n}}) \equiv (\bullet)^{\mathrm{n}}, \quad (\bullet)(\mathrm{t}^{\mathrm{n+1}}) \equiv (\bullet)^{\mathrm{n+1}} \tag{56}$$

Furthermore, taking the arbitrary reference configuration $\mathbf{z}$ to be the $\mathbf{x}^{\mathrm{n}}$ we have

$$\mathbf{z} = \mathbf{x}^{\mathrm{n}}, \quad \mathbf{K}^{\mathrm{n+1}} = \frac{\partial \mathbf{x}^{\mathrm{n+1}}}{\partial \mathbf{x}^{\mathrm{n}}} = \mathbf{F}^{\mathrm{n+1}} \left(\mathbf{F}^{\mathrm{n}}\right)^{-1}, \quad \mathbf{K}^{\mathrm{n}} = \mathbf{1} \tag{57}$$

substitution of (57) in (55) yields

$$\mathbf{B}_{\mathrm{B}}^{\mathrm{n+1}} = \mathbf{K}^{\mathrm{n+1}} \left(\mathbf{1} - 2(\mathrm{t}^{\mathrm{n+1}} - \mathrm{t}^{\mathrm{n}})\mathbf{D}_{\mathrm{B}}^{\mathrm{n}}\right) \mathbf{B}_{\mathrm{B}}^{\mathrm{n}} \left(\mathbf{K}^{\mathrm{n+1}}\right)^{\mathrm{T}} \tag{58}$$

We assume now that variables $\mathbf{F}^{\mathrm{n}}$, $\mathbf{B}^{\mathrm{n}}$, $\mathbf{D}^{\mathrm{n}}$, $\mathbf{B}_{\mathrm{B}}^{\mathrm{n}}$, $\mathbf{D}_{\mathrm{B}}^{\mathrm{n}}$, $\boldsymbol{\sigma}_{\mathrm{A}}^{\mathrm{n}}$, $\boldsymbol{\sigma}_{\mathrm{B}}^{\mathrm{n}}$ are known. Besides, the deformation gradient $\mathbf{F}^{\mathrm{n+1}}$ is provided by the code. Then, we update variables at time $\mathrm{t}^{\mathrm{n+1}}$ as follows

$$\mathbf{B}^{\mathrm{n+1}} = \mathbf{F}^{\mathrm{n+1}} \left(\mathbf{F}^{\mathrm{n+1}}\right)^{\mathrm{T}} \tag{59}$$

$$\mathbf{K}^{\mathrm{n+1}} = \mathbf{F}^{\mathrm{n+1}} \left(\mathbf{F}^{\mathrm{n}}\right)^{-1} \tag{60}$$

$$\mathbf{B}_{\mathrm{B}}^{\mathrm{n+1}} = \mathbf{K}^{\mathrm{n+1}} \left(\mathbf{1} - 2(\mathrm{t}^{\mathrm{n+1}} - \mathrm{t}^{\mathrm{n}})\mathbf{D}_{\mathrm{B}}^{\mathrm{n}}\right) \mathbf{B}_{\mathrm{B}}^{\mathrm{n}} \left(\mathbf{K}^{\mathrm{n+1}}\right)^{\mathrm{T}} \tag{61}$$

$$\boldsymbol{\sigma}_{\mathrm{A}}^{\mathrm{n+1}} = 2\left(\mathrm{I}_3^{\mathrm{n+1}}\right)^{-1/2} \left(\left(\mathrm{I}_3^{\mathrm{n+1}}\mathrm{a} - \mathrm{b}\right)\mathbf{1} + \left(\psi_1^{\mathrm{n+1}} + \mathrm{I}_1^{\mathrm{n+1}}\psi_2^{\mathrm{n+1}}\right)\mathbf{B}^{\mathrm{n+1}} - \psi_2^{\mathrm{n+1}}\left(\mathbf{B}^{\mathrm{n+1}}\right)^2\right) \tag{62}$$

$$\boldsymbol{\sigma}_{\mathrm{B}}^{\mathrm{n+1}} = 2\left(\mathrm{I}_{\mathrm{B3}}^{\mathrm{n+1}}\right)^{-1/2} \left(\left(\mathrm{I}_{\mathrm{B3}}^{\mathrm{n+1}}\mathrm{a}_{\mathrm{B}} - \mathrm{b}_{\mathrm{B}}\right)\mathbf{1} + \left(\psi_{\mathrm{B1}}^{\mathrm{n+1}} + \mathrm{I}_{\mathrm{B1}}^{\mathrm{n+1}}\psi_{\mathrm{B2}}^{\mathrm{n+1}}\right)\mathbf{B}_{\mathrm{B}}^{\mathrm{n+1}} - \psi_{\mathrm{B2}}^{\mathrm{n+1}}\left(\mathbf{B}_{\mathrm{B}}^{\mathrm{n+1}}\right)^2\right) \tag{63}$$

$$\mathbf{D}_{\mathrm{B}}^{\mathrm{n+1}} = \frac{2}{9\eta_1}(\mathrm{tr}\boldsymbol{\sigma}_{\mathrm{B}}^{\mathrm{n+1}})\mathbf{1} + \frac{1}{\eta_2^{\mathrm{n+1}}}\mathrm{dev}\boldsymbol{\sigma}_{\mathrm{B}}^{\mathrm{n+1}} \tag{64}$$

To remove the failed element the following condition should be obeyed at one of the element Gauss points

$$\mathrm{H}(\xi^{\mathrm{n+1}}) = 0 \tag{65}$$

where

$$\xi^{\mathrm{n+1}} = -(\mathrm{t}^{\mathrm{n+1}} - \mathrm{t}^{\mathrm{n}})\mathrm{H}\left(\varepsilon - \frac{\left(\psi_{\mathrm{A}}^{\mathrm{e}}\right)^{\mathrm{n+1}}}{\left(\psi_{\mathrm{A}}^{\mathrm{f}}\right)^{\mathrm{n+1}}}\right) + \xi^{\mathrm{n}}, \quad \xi^0 = 0 \tag{66}$$

5 Numerical simulations

In this section we show sample finite element computations conducted in ABAQUS/Explicit which illustrate the joint performance of the constitutive model and the integration algorithm. The calculations simulate the dynamic tension tests performed by Hoo Fatt and Ouyang (2008).

5.1 Finite element model

Fig. 3 shows the ASTM D638 type IV dumbbell specimen used in the experiments of Hoo Fatt and Ouyang (2008). In the numerical calculations, due to the symmetry of the model, we have only modeled 1/4 of the specimen. The finite element model is initially at rest and unstretched. The mechanical boundary conditions are shown in Fig. 3, where $\mathrm{u_i}$ are the components of the displacement vector $\mathbf{u}$, θ_{i} are the components of the rotation vector $\boldsymbol{\theta}$ and $\mathrm{v}_1 = \mathrm{v}^{\mathrm{imp}}$ is the impact (loading) velocity.

The finite element model has been meshed using a total of 7560 eight-node solid elements with reduced integration and hourglass control, C3D8R in ABAQUS notation. Three elements are placed through the thickness of the model. In the gauge of the specimen, the elements show an aspect ratio $0.2 : 1 : 1$. Short elements along the axial direction are required to capture (accurately) the failure of the specimen since the material undergoes large axial strains ($\lambda > 5$)

before fracture. Elements with larger axial dimension are badly stretched by the time of fracture and the failure process is not properly described. Furthermore, a mesh convergence study was performed, in which the time evolution of the stress, strain and strain rate fields were compared against a measure of mesh density until the results converged satisfactorily. We hold that viscosity and inertia act as regularization factors that contribute to the well-possessedness of the problem, see Molinari (1997) and Needleman (2008). We assume that this minimizes the spurious influence of the mesh in the solution of the boundary value problem.

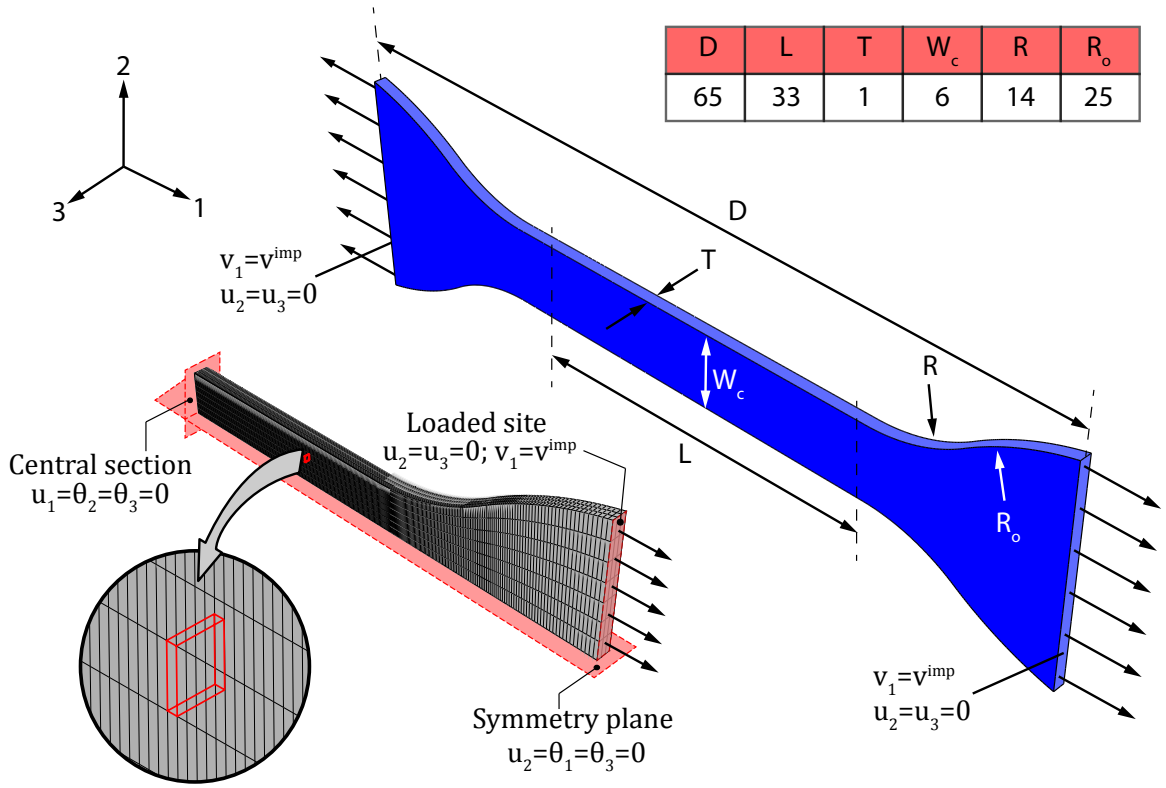

D	L	T	W_c	R	R_o
65	33	1	6	14	25

Figure 3: Geometry and dimensions (in mm) of the ASTM D638 type IV dumbbell specimen. Finite element model, mesh and mechanical boundary conditions applied in the calculations.

5.2 Sample results

Fig. 4 compares the experimental (axial) stress-stretch curves reported by Hoo Fatt and Ouyang (2008) with our finite element calculations. In the computations the stress is calculated as $\sigma = \frac{\mathrm{F}}{\mathrm{A}_0}\lambda$ where F is the axial force measured in the loaded site of the model, A_0 is the initial cross-section area of the gauge and λ is the axial stretch calculated measuring the increase in length of the sample gauge referred to as L in Fig. 3. The stretch rate which denotes each loading case in the simulations corresponds to the (average) value of $\dot{\lambda}$ registered in the specimen gauge during the calculations. The maximum stretch shown in the numerical results corresponds to the onset of failure. Beyond this point, the stress state is no longer uniaxial. The agreement between experiments and numerical calculations reveals the satisfactory performance of the (simple) integration algorithm presented in the previous section.

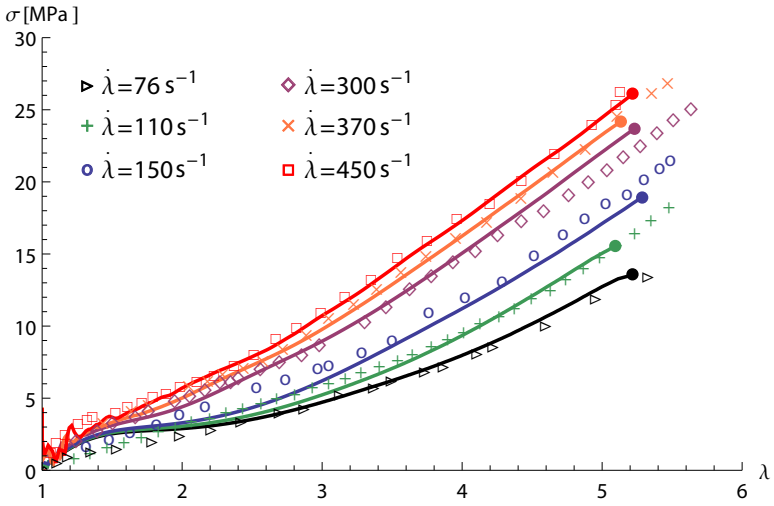

Figure 4: Comparison between the numerical calculations (solid lines) and the experiments (markers) performed by Hoo Fatt and Ouyang (2008). Unixiaxial (Cauchy) stress-stretch curves ($\sigma - \lambda$). Various stretch rates are considered: $76\,\mathrm{s}^{-1}$, $110\,\mathrm{s}^{-1}$, $150\,\mathrm{s}^{-1}$, $300\,\mathrm{s}^{-1}$, $370\,\mathrm{s}^{-1}$and $450\,s^{-1}$.

Fig. 5 illustrates force-time curves ($\mathrm{F} - \mathrm{t}$) measured at both ends of the model: loaded site and central section (see Fig. 3). The applied stretch rate is $76\,\mathrm{s}^{-1}$. We observe that both curves practically overlap each other. The specimen is largely equilibrated. The only difference resides at the very beginning of loading when inertia effects lead to slight fluctuations in the force recorded in the loaded site.

The force first increases and reaches a local maximum for $\mathrm{t} \approx 0.005\,\mathrm{s}$ which leads to localization of deformation in the gauge, see Fig. 6. The local maximum corresponds to the attainment of the Considère condition. Beyond the local maximum, the deformation tends to increase quickly until a minimum is reached in the $\mathrm{F} - \mathrm{t}$ curve for $\mathrm{t} \approx 0.012\,\mathrm{s}$. The minimum corresponds to the change of curvature in the corresponding $\sigma - \lambda$ characteristic shown in Fig. 4. The subsequent increase in strength stabilizes the flow stress leading to largely uniform distributions of stretch (Fig. 6) and stretch rate (Fig. 7) within the gauge of the specimen. Heterogeneity in the field variables is just observed immediately before the maximum force is reached for $\mathrm{t} \approx 0.046\,\mathrm{s}$, see Figs. 6 and 7. Then, rapid localization of deformation occurs within a small zone of the sample gauge leading to material failure.

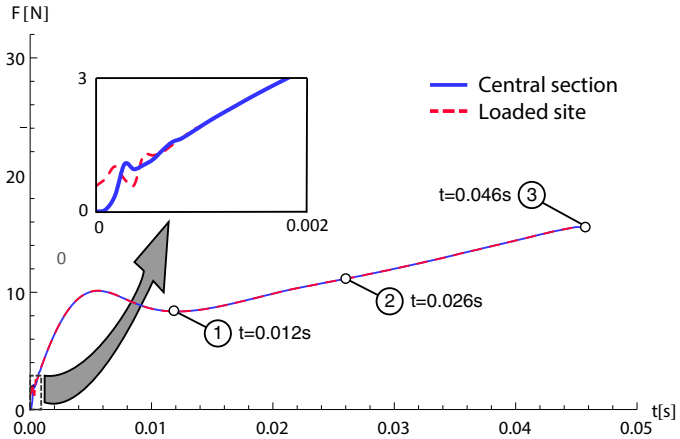

Figure 5: Finite element calculations. Force-time curves ($\mathrm{F} - \mathrm{t}$) measured at both ends of the model: loaded site and central section. The applied stretch rate is $76\,\mathrm{s}^{-1}$.

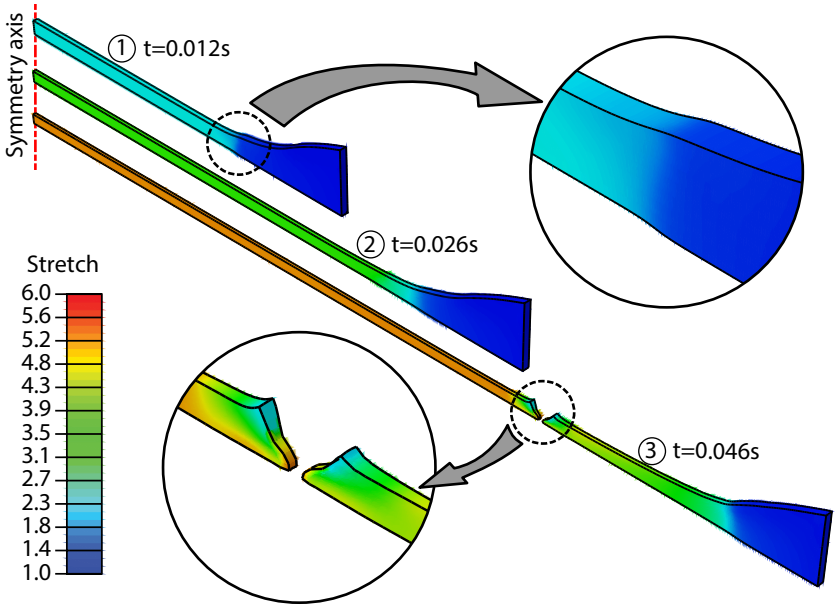

Figure 6: Finite element calculations. Contours of axial stretch λ. The applied stretch rate is $76\,\mathrm{s}^{-1}$.

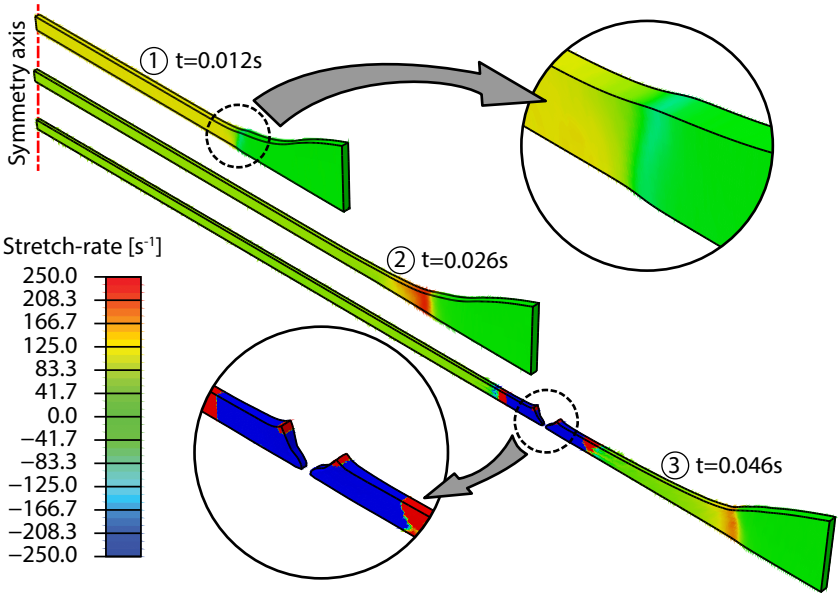

Figure 7: Finite element calculations. Contours of axial stretch rate $\dot{\lambda}$. The applied stretch rate is $76\,\mathrm{s}^{-1}$.

Fig. 8 shows force-time curves ($\mathrm{F}-\mathrm{t}$) measured at the loaded site and the central section. The applied stretch rate is $450\,\mathrm{s}^{-1}$, the highest explored in this paper. At the beginning of loading we observe significant fluctuations in the force which are caused by the propagation of stress waves within the specimen. It is apparent that, for this loading rate, inertia effects are meaningful. The stretch rate fields within the specimen are rather heterogeneous, see Fig. 10. These fluctuations are progressively attenuated and, for $\mathrm{t} \geq 0.002\,\mathrm{s}$, both curves become practically coincident (the specimen is largely equilibrated) and the field variables show uniform distributions along the gauge (see Figs. 9 and 10). A maximum in the $\mathrm{F}-\mathrm{t}$ curves is reached for $\mathrm{t} \approx 0.0094\,\mathrm{s}$ which leads to fast strain localization and subsequent material failure.

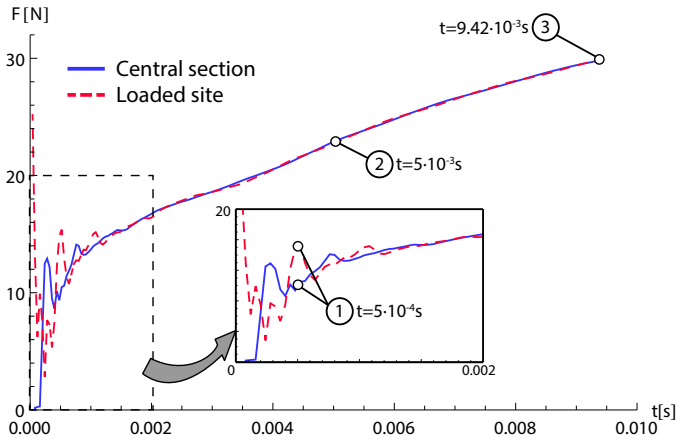

Figure 8: Finite element calculations. Force-time curves (F − t) measured at both ends of the sample: loaded site and central section. The applied stretch rate is $450\,\mathrm{s}^{-1}$.

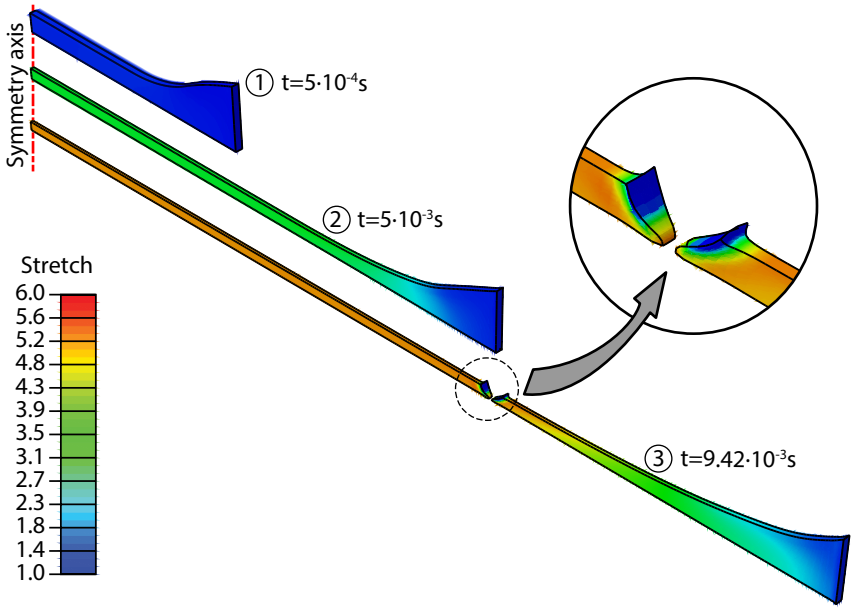

Figure 9: Finite element calculations. Contours of axial stretch λ. The applied stretch rate is $450\,\mathrm{s}^{-1}$.

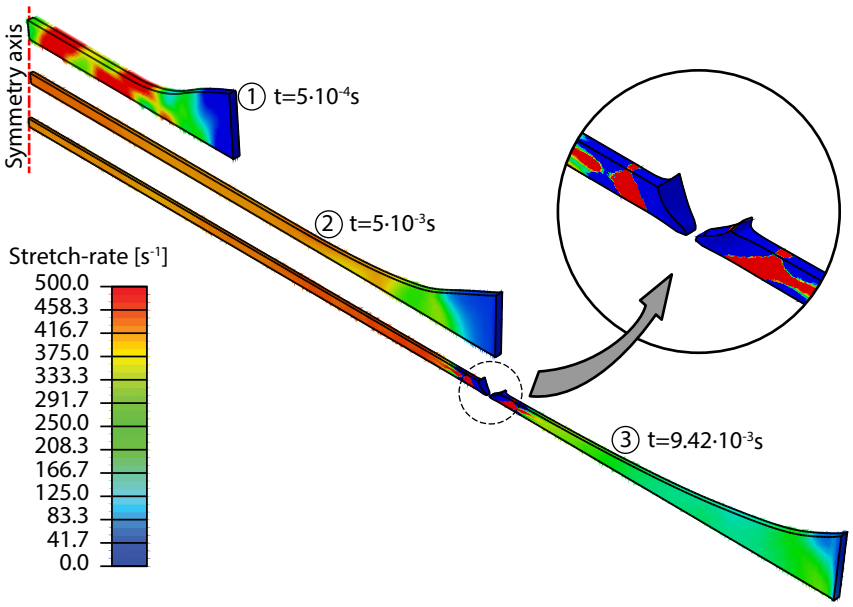

Figure 10: Finite element calculations. Contours of axial stretch rate $\dot{\lambda}$. The applied stretch rate is $450\,\mathrm{s}^{-1}$.

These numerical examples demonstrate the ability of the constitutive model and the integration algorithm developed in this paper to simulate deformation and failure of structures (or components, or parts...) manufactured with non-linear viscoelastic materials and subjected to dynamic loading.

6 Concluding remarks

In this work we have developed a new viscoelastic constitutive model to describe deformation and failure of elastomers subjected to high strain rates. The model has been calibrated for styrene butadiene rubber using experimental data reported in the literature and implemented into ABAQUS/Explicit via a user subroutine. Finite element simulations of dynamic tensile experiments reported by Hoo Fatt and Ouyang (2008) have been carried out to exemplify the joint performance of the constitutive model and the integration algorithm. The simplicity of the constitutive theory and the efficiency of the implementation scheme make the formulation developed in this research especially suited to study engineering applications in which rate-dependent rubber-like materials are subjected to dynamic deformation and failure.

Acknowledgment

DAI, GV and JARM are indebted to the Spanish Ministry of Economy and Competitiveness (Projects EUIN2015-62556 and DPI2014-57989-P) for the financial support received which allowed conducting part of this work.

KYV acknowledges support from the Israel Science Foundation, grant No. ISF-198/15.

References

Amin, A., Lion, A., Sekita, S., Okui, Y., 2006. Nonlinear dependence of viscosity in modeling the rate-dependent response of natural and high damping rubbers in compression and shear: Experimental identification and numerical verification. International Journal of Plasticity 22 (9), 1610–1657.

Bergström, J., Boyce, M., 1998. Constitutive modeling of the large strain time-dependent behavior of elastomers. Journal of the Mechanics and Physics of Solids 46 (5), 931–954.

Carreau, P. J., De Kee, D., Chhabra, R. P., 1997. Rheology of polymeric systems: principles and applications. Hanser Publishers Munich.

Eckart, C., 1948. The thermodynamics of irreversible processes. IV. The theory of elasticity and anelasticity. Physical Review 73, 373–382.

Govindjee, S., Reese, S., 1997. A presentation and comparison of two large deformation viscoelasticity models. Journal of Engineering Materials and Technology 119 (3), 251–255.

Green, A. E., Rivlin, R. S., 1957. The mechanics of non-linear materials with memory, part i. Archive for Rational Mechanics and Analysis (1), 1–21.

Green, A. E., Rivlin, R. S., 1960. The mechanics of non-linear materials with memory, part iii. Archive for Rational Mechanics and Analysis (4), 387–404.

Hoo Fatt, M. S., Ouyang, X., 2007. Integral-based constitutive equation for rubber at high strain rates. International Journal of Solids and structures 44 (20), 6491–6506.

Hoo Fatt, M. S., Ouyang, X., 2008. Three-dimensional constitutive equations for styrene butadiene rubber at high strain rates. Mechanics of Materials 40, 1–16.

Huber, N., Tsakmakis, C., 2000. Finite deformation viscoelasticity laws. Mechanics of materials 32 (1), 1–18.

Leonov, A. L., 1976. Nonequilibrium thermodynamics and rheology of viscoelastic polymer media. Rheologicl Acta 15, 85–98.

Lion, A., 1996. A constitutive model for carbon black filled rubber: experimental investigations and mathematical representation. Continuum Mechanics and Thermodynamics 8 (3), 153–169.

Lockett, F. J., 1972. Nonlinear viscoelastic solids. Academic Press.

Lopez-Pamies, O., 2010. A new I1-based hyperelastic model for rubber elastic materials. Comptes Rendus Mecanique 338 (1), 3–11.

Lubliner, J., 1985. A model of rubber viscoelasticity. Mechanics Research Communications 12 (2), 93–99.

Miehe, C., Keck, J., 2000. Superimposed finite elastic–viscoelastic–plastoelastic stress response with damage in filled rubbery polymers. experiments, modelling and algorithmic implementation. Journal of the Mechanics and Physics of Solids 48 (2), 323–365.

Molinari, A., 1997. Collective behaviour and spacing of adiabatic shear bands. Journal of the Mechanics and Physics of Solids 45, 1551–1575.

Needleman, A., 2008. Material rate dependence and mesh sensitivity in localization problems. Computer Methods in Applied Mechanics and Engineering 67, 69–85.

Quintavalla, S., Johnson, S., 2004. Extension of the bergstrom-boyce model to high strain rates. Rubber Chemistry and Technology 77 (5), 972–981.

Reese, S., Govindjee, S., 1998. A theory of finite viscoelasticity and numerical aspects. International Journal of Solids and Structures 35 (26), 3455–3482.

Shim, V., Yang, L., Lim, C., Law, P., 2004. A visco-hyperelastic constitutive model to characterize both tensile and compressive behavior of rubber. Journal of Applied Polymer Science 92 (1), 523–531.

Trapper, P., Volokh, K. Y., 2010. Modeling dynamic failure in rubber. International Journal of Fracture 162 (1), 245–253.

Volokh, K., 2004. Nonlinear elasticity for modeling fracture of isotropic brittle solids. Journal of applied mechanics 71 (1), 141–143.

Volokh, K., 2007. Hyperelasticity with softening for modeling materials failure. Journal of the Mechanics and Physics of Solids 55 (10), 2237–2264.

Volokh, K., 2010. On modeling failure of rubber-like materials. Mechanics Research Communications 37 (8), 684–689.

Volokh, K., 2011. Modeling failure of soft anisotropic materials with application to arteries. Journal of the Mechanical Behavior of Biomedical Materials 4 (8), 1582–1594.

Volokh, K., 2013a. An approach to elastoplasticity at large deformations. European Journal of Mechanics-A/Solids 39, 153–162.

Volokh, K., 2013b. Review of the energy limiters approach to modeling failure of rubber. Rubber Chemistry and Technology 86 (3), 470–487.

Volokh, K., 2014. On irreversibility and dissipation in hyperelasticity with softening. Journal of Applied Mechanics 81 (7), 074501.

Volokh, K., Trapper, P., 2008. Softening hyperviscoelasticity for modeling rate-dependent material failure. Journal of Mechanics of Materials and Structures 3 (9), 1695–1707.

Wineman, A., 2009. Nonlinear viscoelastic solids-a review. Mathematics and Mechanics of Solids 14 (3), 300–366.

Yang, L., Shim, V., Lim, C., 2000. A visco-hyperelastic approach to modelling the constitutive behaviour of rubber. International Journal of Impact Engineering 24 (6), 545–560.